Characterisation of flexible fibre deformations in turbulence

A. Gay, B. Favier and G. Verhille [(a)]

Aix Marseille Univ, CNRS, Centrale Marseille, IRPHE, Marseille, France

PACS 47.27.-i – Turbulent flows
PACS 47.55.Kf – Particle-laden flows
PACS 47.57.Ng – Polymers and polymer solutions

Abstract – The transport of deformable objects by a turbulent flow is common in environmental sciences which are interested for instance by the dynamics of plankton in the ocean, and in industry, such as the papermaking or textile industries. In this study, the deformations of flexible fibres in homogeneous isotropic turbulence are experimentally and numerically investigated, focusing on the local curvature κ. By comparing our results to the predictions for worm-like chain polymers in an ideal solvent, we are able to identify the role of the spatial and temporal correlations of the turbulent forcing. In particular, we show that these correlations are responsible for a straightening of long fibres which become statistically less distorted by turbulence as their length increases.

Introduction. Particle advection in turbulence is common in industrial processes, *e.g.* papermaking [1], and in natural phenomena with the transport of plankton in ocean [2] or the dispersion of pollen species in the atmosphere [3]. The Lagrangian dynamics of particles was extensively studied, exploring the properties of isotropic or anisotropic rigid objects [4,5]. Recent studies highlighted the importance of particle shape on the transport. For instance, the rotation rate of small axisymmetric anisotropic particles depends on their aspect ratio [6,7]. One can then address the question of the transport of flexible objects, such as plankton in the ocean or pulp fibres in the papermaking industry, for which the shape may evolve with time depending on the external stresses. Several studies considered the case of flexible fibres at low Reynolds numbers [8, 9] but very little is known about the motion of such objects when the flow is turbulent.

Inspired by flexible objects in nature or industrial processes which can often be considered as one-dimensional elongated objects, this study is focused on flexible fibres in Homogeneous and Isotropic Turbulence (HIT). Their dynamics should be determined by their time-dependent shape which is related to their deformations due to the turbulent viscous stresses. This letter is focused on the characterisation of the fibre deformations which is a first step to understand their dynamics. As the fibre extensibility and torsion are second order effects with respect to the bending [10], we only consider the bending deformations. Following Kirchhoff-Love theory and Euler-Bernoulli elasticity, their dynamics is then given by [11–13]

$$\sigma\partial_t^2\boldsymbol{r} - \partial_s\left(T\partial_s\boldsymbol{r}\right) + B\partial_s^4\boldsymbol{r} = \boldsymbol{\xi}\ , \tag{1}$$

where $\boldsymbol{r}$ is the position of the fibre centre line, $\boldsymbol{\xi}$ an external forcing and s the curvilinear coordinate. σ and B are, respectively, the linear density and the bending modulus of the fibre, all assumed to be constant along the fibre. T is a tension term acting as a Lagrange multiplier in order to ensure the fibre inextensibility ($|\partial_s\boldsymbol{r}| = 1$). It is expected that this system shares some similarities with worm-like chain polymers as their idealised equations of motion are similar [14, 15].

The crucial difference between polymers in a thermal bath and fibres in a turbulent flow lies in the nature of the linear forcing term $\boldsymbol{\xi}$. Assuming that the particle Reynolds number is small and ignoring the anisotropic nature of the viscous drag for slender bodies, we have $\boldsymbol{\xi} \simeq 4\pi\eta(\ln 2\lambda)^{-1}\boldsymbol{u}_{\rm slip}$ [16] where η is the fluid dynamical viscosity, $\lambda = L/d$ the aspect ratio between the fibre length L and its diameter d, and $\boldsymbol{u}_{\rm slip} = \boldsymbol{u} - \partial_t\boldsymbol{r}$ the slip velocity between the fluid and the fibre. For the polymer regime, we assume that the forcing is effectively delta correlated in space and time

$$\langle\boldsymbol{u}(\boldsymbol{x}+\boldsymbol{s}, t+\tau)\cdot\boldsymbol{u}(\boldsymbol{x}, t)\rangle = u_{\rm rms}^2\delta(\tau)\delta(\boldsymbol{s})\ , \tag{2}$$

where $\langle\cdot\rangle$ corresponds to an ensemble average. For stationary HIT, the fluid velocity $\boldsymbol{u}$ is spatially and temporally correlated in the inertial range. This result is at the origin

[(a)] E-mail: gautier.verhille@irphe.univ-mrs.fr

of the classical Kolmogorov 4/5 law [17]:

$$\left\langle [(\boldsymbol{u}(\boldsymbol{x}+\boldsymbol{\chi})-\boldsymbol{u}(\boldsymbol{x}))\cdot\boldsymbol{e}_\chi]^3 \right\rangle = -\frac{4}{5}\epsilon\chi, \tag{3}$$

where ϵ is the dissipation rate of the turbulent kinetic energy per unit mass and $\boldsymbol{e}_\chi = \boldsymbol{\chi}/|\boldsymbol{\chi}|$.

Using the integral length scale L_I and the root mean square velocity of the turbulence U as references, a dimensionless version of equation (1) is

$$\partial_t^2\boldsymbol{r} - \partial_s\left(T\partial_s\boldsymbol{r}\right) + \gamma\partial_s^4\boldsymbol{r} + \frac{1}{St}\partial_t\boldsymbol{r} = \frac{1}{St}\boldsymbol{u}\ . \tag{4}$$

The fibre dynamics depends on two dimensionless parameters: a Stokes number

$$St = \sigma U/\left[4\pi\eta(\ln(2\lambda))^{-1}L_I\right]\ , \tag{5}$$

which compares the inertial term $\sigma\partial_{tt}\boldsymbol{r}$ and the viscous term $4\pi\eta(\ln 2\lambda)^{-1}\partial_t\boldsymbol{r}$ and a dimensionless rigidity γ which compares the inertial term and the bending term $B\partial_s^4\boldsymbol{r}$:

$$\gamma = B/\left(\sigma U^2 L_I^2\right)\ . \tag{6}$$

In polymer science, the deformations of worm-like chain polymers are classically characterised by the persistence length ℓ_p defined by $\mathcal{C}(\ell) \equiv \langle \boldsymbol{t}(s+\ell)\cdot\boldsymbol{t}(s)\rangle = e^{-\ell/\ell_p}$ where $\boldsymbol{t} = \partial_s\boldsymbol{r}/|\partial_s\boldsymbol{r}|$ is the unit tangent vector. This length is generally related to a balance between the elastic energy and the thermal energy $B/\ell_p \sim k_BT$ where k_B is the Boltzmann constant and T the bath temperature [18]. By measuring the distance between fibre extremities, Brouzet *et al.* [19] showed that the same approach may be applied to fibres in turbulence. However, in the inertial range, the persistence length cannot be modelled from an energy balance since the fibre dynamics and the forcing occur on different timescales. Thus, they used a power balance to define a new characteristic length called the elastic length

$$\ell_e = B^{1/4}/(\rho_f\eta\epsilon)^{1/8}\ , \tag{7}$$

where ρ_f is the fluid density. The transition from rigid to flexible fibres is then governed by the ratio of the fibre length L to the elastic length ℓ_e: for $L < \ell_e$ (resp. $L > \ell_e$) the fibre deformations are weak (resp. large), *i.e.* the averaged distance between the fibre extremities is nearly equal to (resp. much smaller than) the fibre length L. To investigate this analogy, Verhille and Bartoli [20] performed a 3D experimental reconstruction analysis to measure the correlation function $\mathcal{C}(\ell)$. They observed that the correlation function is well described by an exponential law $\mathcal{C}(\ell) \sim e^{-\ell/\ell_p}$ for $\ell > \ell_e$. However, in turbulence, and contrary to polymers, the persistence length ℓ_p depends on the fibre length L itself and cannot be assimilated to the elastic length. The main objective of this letter is to understand this phenomenon by investigating the role of the spatial correlations of the forcing.

Several regimes are expected depending on the ratio between the fibre length scales (its length L and elastic length ℓ_e) and the flow length scales (the integral scale L_I and the Kolmogorov scale η_K). In the following, we assume that all fibre scales are much larger than the Kolmogorov scale and that fibres are flexible ($L > \ell_e$). Therefore, three different regimes can be distinguished (see fig. 1). In a first regime, the integral scale is much smaller than the elastic length ($L > \ell_e \gg L_I$), so that the forcing is effectively uncorrelated at the scale of the fibre deformations (neglecting for simplicity spatial correlations at scales larger than L_I). This is called the polymer regime, for which the turbulent fluctuations can be seen as a thermal bath since it is only correlated at scales much smaller than the relevant elastic scale. Note that physically the elastic length ℓ_e, derived in the inertial range, is not pertinent for this regime and should be replaced by a persistence length ℓ_p as done in polymer science [18]. In a second case, the fibre length lies in the inertial range ($L_I \gg L > \ell_e$) and the forcing is now correlated along the fibre. This case is called the turbulent regime. Finally the last case is an intermediate regime ($L > L_I > \ell_e$) for which the fibre experiences a forcing correlated at small scale but uncorrelated at the larger scale. Both turbulent and intermediate regimes were largely unexplored up to now. In this letter, we investigate experimentally and numerically the evolution of the local curvature $\kappa(s) = |\partial_s\boldsymbol{t}(s)|$ of a flexible but inextensible fibre. It is natural to focus on the local curvature since it gives access to the elastic energy stored in the fibre $\mathcal{E}_B = (1/2)B\int\kappa^2(s)\mathrm{d}s$ and is also related to the correlation function $\mathcal{C}(\ell) \simeq 1 - \langle\kappa^2\rangle\ell^2/2 + \mathcal{O}(\ell^3)$.

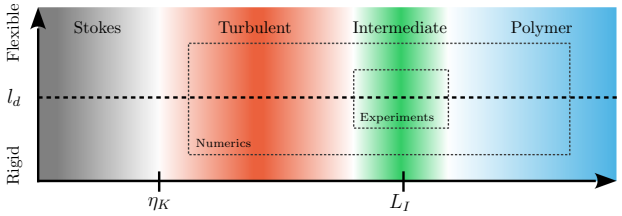

Fig. 1: Schematic comparing the fibre length L with the different length scales in the problem from largest fibres behaving like polymers ($L \gg L_I$) down to small fibres in the Stokes regime ($L \ll \eta_K$). η_K is the Kolmogorov length scale and L_I the integral scale of the homogeneous isotropic turbulent flow. We focus on a new turbulent regime where $\eta_K \ll L \ll L_I$. The vertical axis shows the fibre length versus l_d, the typical length above which elastic deformations become significant. In the turbulent regime of interest here, $l_d = \ell_e$ as discussed in the text. The regimes covered by both experiments and numerical models are qualitatively indicated by the dashed boxes.

Materials and methods. We now describe our experimental setup and numerical model. Experimentally, the turbulence is generated within a von Kármán setup similar to the one used in our previous experiments [20] (see fig. 2). It is a water-filled cubic tank (side length 20 cm) with two impellers (R = 8.6 cm in radius fitted with blades)

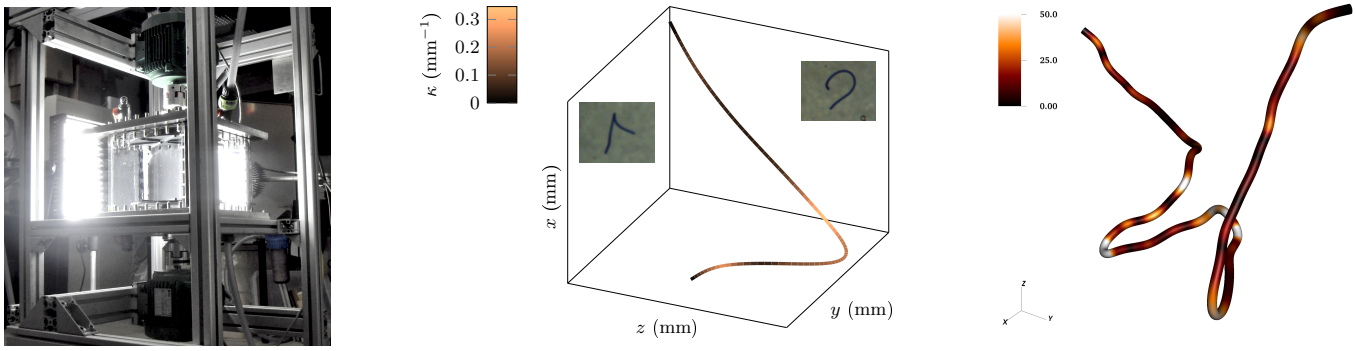

Fig. 2: Left: image of the experimental setup. Middle: example of 3D reconstruction of a fibre conformation from experimental data, the colour codes the curvature $\kappa(s)$. Right: example of a fibre conformation from a numerical simulation in the turbulent regime (the fibre length is smaller than the integral scale), the colour shows the local value of the curvature $\kappa(s)$ normalised by the integral length scale L_I.

counter rotating at a fixed frequency $F = 15$ Hz. The Reynolds number is of the order of $Re = 2\pi R^2 F/\nu \sim 8 \times 10^5$, the integral scale $L_I \sim R$ and the Kolmogorov length $\eta_K \sim 40$ μm. The fibres are made of silicone with a Young modulus $E = 40 \pm 15$ kPa and a density $\rho = 1.03 \times 10^3$ kg.m^{-3}. They are moulded in a stainless steel tube to tune their diameter to $d = 505 \pm 3$ μm, leading to $\sigma = 2.06 \cdot 10^{-4}$ kg.m^{-1}, and their length L from 1.0 cm to 5.0 cm. The Reynolds number based on the diameter is of the order of $Re_d = (d/\eta_K)^{4/3} \sim 30$. For simplicity, we assume that this value is small enough to consider only the linear Stokes' drag presented in the introduction [21] Their elastic length is equal to $\ell_e = B^{1/4}/(\rho_f \eta \epsilon)^{1/8} = 2.7 \pm 0.4$ mm with $B = \pi E d^4/64 = 1.3 \pm 0.5 \times 10^{-10}$ N.m^2. The Stokes number St is of order of $0.2 - 0.4$ and $\gamma \sim 10^{-4}$. The comparison between the different length scales shows that only the intermediate regime is achievable experimentally with the current setup. The turbulent regime would require a much larger integral scale or much more flexible objects, both of which being challenging experimentally. Two IDS UI-5240CP-C-HQ cameras with 25 mm lens are used to capture the motion of the fibres at two different angles. The images are then processed to determine the fibre 3D shape thanks to an optimised version of the algorithm proposed by Verhille and Bartoli [20]. A typical fibre 3D shape is shown in fig. 2. To increase the contrast we used a LED-panel back-light. These light sources allow us to image fibres with an exposure time of 0.3 ms, chosen to avoid motion blur, and at a maximum frequency of 5 images per second. The relatively low acquisition rate is justified since we only focus on the statistical properties of the fibre curvature, not on its dynamics.

Since the turbulent regime cannot be achieved experimentally using our current setup, we also rely on an idealised numerical model. For the elastic part of the problem, we solve equation (4) using a numerical scheme directly inspired from previous studies on flexible fibres [22–24]. Spatial derivatives are approximated using sixth-order finite differences on a staggered grid and we use a semi-implicit backward difference temporal scheme of third order [25], the bending term being solved implicitly while the other terms are solved explicitly. We typically use between 128 and 2048 grid points regularly distributed along the fibre. The inexensibility of the fibre leads to a Poisson-type equation on the tension T, which is solved at each time step. We have checked that the relative error on the fibre length is typically smaller than 10^{-5} for all cases discussed here. Concerning the fluid flow, and contrary to previous methods considering Stokes flows [22] or using Immersed Boundary Methods [26], our fluid velocity $\boldsymbol{u}$ is obtained analytically as a superposition of incompressible random Fourier modes. This method, often called Kinematic Simulation [27], has a long history [28] and was used in various Lagrangian studies [29, 30]. Although the flow is not a solution of the Navier-Stokes equations, it is rigorously incompressible and its second-order statistics can be finely tuned to mimic those of realistic turbulence. All the results shown in this paper are obtained using 10^3 incompressible Fourier modes whose two-point correlations are derived from an energy spectrum given by $E(k) = C_k \epsilon^{2/3} k^{-5/3}$ and using a typical eddy turnover time $\omega(k) = 1/2\sqrt{k^3 E(k)}$ [31]. In all cases, our synthetic turbulent flow is defined over three decades of wave numbers, thus ensuring ample scale separation between the integral and Kolmogorov scales. For simplicity, we neglect correlations at scales larger than the integral scale, thus idealising the transition between the turbulent and polymer regimes. Note that the results do not qualitatively depend on these particular choices, only the spatial correlations and therefore the amplitude and slope of the energy spectrum matter. As mentioned in the introduction, the viscous forcing is assumed isotropic (which is not the case for a slender body, see [10, 32]). We have checked that this assumption does not change qualitatively the different results presented here. Note that solving the full two-way coupling between the elastic fibre and the

turbulent flow using Direct Numerical Simulations (DNS) would be a tremendous task, which we leave for future works, whereas our simple approach allows us to consider many realisations of the same input parameters. Finally, the dimensionless elastic length can be defined as:

$$(\ell_e/L_I)^8 = (\sigma/\rho_f L_I^2)\gamma^2 St \approx \gamma^2 St \ , \qquad (8)$$

where the prefactor $\sigma/\rho_f L_I^2$ is constant and of order unity for all the numerical simulations discussed below (the fibre is assumed to have the same density of the fluid and in the experiment $(\sigma/\rho_f L_I^2)^{1/8} \sim 0.3$ justifying the approximation made here). We used $St = 0.1$ and different fibre rigidities γ from 10^{-6} to 10^6, noting that different values of the Stokes number do not qualitatively change the results discussed in this letter. In the following, we particularly focus on three cases: $\gamma = 10^3$ which corresponds to the polymer regime ($\ell_e/L_I \approx 4.2$), $\gamma = 0.2$ which corresponds to the intermediate regime ($\ell_e/L_I \approx 0.5$) and $\gamma = 10^{-5}$ which corresponds to the turbulent regime ($\ell_e/L_I \approx 0.042$). All the numerical results are obtained after time averaging during the quasi-steady state over tens of turnover times and over 10^2 independent realisations. An example of a fibre conformation from a numerical simulation in the turbulent regime can be seen in Fig. 2.

Results. We first discuss the evolution of the mean squared distance between the fibre extremities $\langle {R_e}^2 \rangle = \langle |\boldsymbol{r}(s=0) - \boldsymbol{r}(s=L)|^2 \rangle$. Within the worm-like chain assumption, this quantity is related to the fibre length L and the persistence length ℓ_p [18]:

$$\langle R_e^2 \rangle = 2\ell_p^2 - 2L\ell_p \left(1 - \mathrm{e}^{-L/\ell_p}\right) \ . \qquad (9)$$

Figure 3 represents the evolution of the mean squared distance between the fibre extremities $\langle R_e^2 \rangle$ as a function of the fibre length L both normalised by the persistence length, determined by fitting expression (9) to our data. We can observe that all the experimental and numerical points are very close to the worm-like chain prediction, as already observed by [19]. However, for the longest fibres in the turbulent regime, equation (9) tends to underestimate the values observed in our numerical model. This indicates that the forcing correlations play a role in the deformations. Our observations show that the global quantity R_e is not sensitive enough to investigate the influence of the correlations of the forcing, as mentioned by [20]. This is why we now focus on the evolution of the mean curvature as a function of the fibre length in the different regimes. Since the boundary conditions impose a curvature $\kappa = 0$ at the fibre extremities, we compute the mean value of the curvature as:

$$\bar{\kappa} = 1/(L - 2\ell_e) \int_{\ell_e}^{L-\ell_e} \langle \kappa(s) \rangle \mathrm{d}s \ . \qquad (10)$$

This allows to remove effects from the fibre extremities where the curvature rapidly increases (see fig. 4).

Otherwise, for short rigid fibres with $L < \ell_e$, the mean value is taken as the maximum of the mean curvature

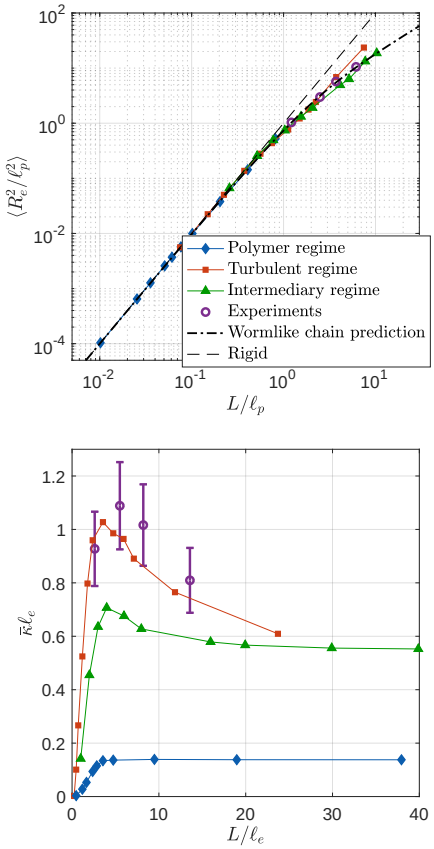

Fig. 3: Top: Evolution of the mean squared distance between fibre extremities R_e^2 as a function of the fibre length L, both quantities being normalised by the persistence length ℓ_p. The dot-dashed line represents the worm-like chain prediction and the dashed line the evolution for rigid fibres. Bottom: Evolution of the fibre mean curvature $\bar{\kappa}$ as a function of the fibre length L both normalised by ℓ_e for the experiments (○, the error bars indicate the uncertainties associated with the fitting process from the 3D reconstructed points), the turbulent regime (■, $\gamma = 10^{-5}$ and $\ell_e/L_I = 4.3 \times 10^{-2}$), the intermediate regime (▲, $\gamma = 0.2$ and $\ell_e/L_I = 0.5$) and the polymer regime (◆, $\gamma = 10^3$ and $\ell_e/L_I = 4.5$).

along the fibre, *i.e.* at the center of the fibre $s = L/2$. This quantity is represented in fig. 3 for both experiments and numerical simulations as a function of the fibre length normalised by the elastic length ℓ_e defined by the power budget. In the polymer regime (◆, $\gamma = 10^3$, $\ell_e/L_I \approx 4.2$), the numerical results are compatible with worm-like chain prediction. The mean curvature increases with the fibre length until it saturates to a constant value independent of the fibre length. The transition length between the two tendencies is nearly the persistence length ℓ_p independent of the fibre length L as it is defined in polymer science. For the turbulent regime (■, $\gamma = 10^{-5}$, $\ell_e/L_I \approx 0.042$) and the intermediate one (▲, $\gamma = 0.2$, $\ell_e/L_I \approx 0.5$), the mean curvature increases with the fibre length L up to a maximum after which it decreases. This effect is also observed

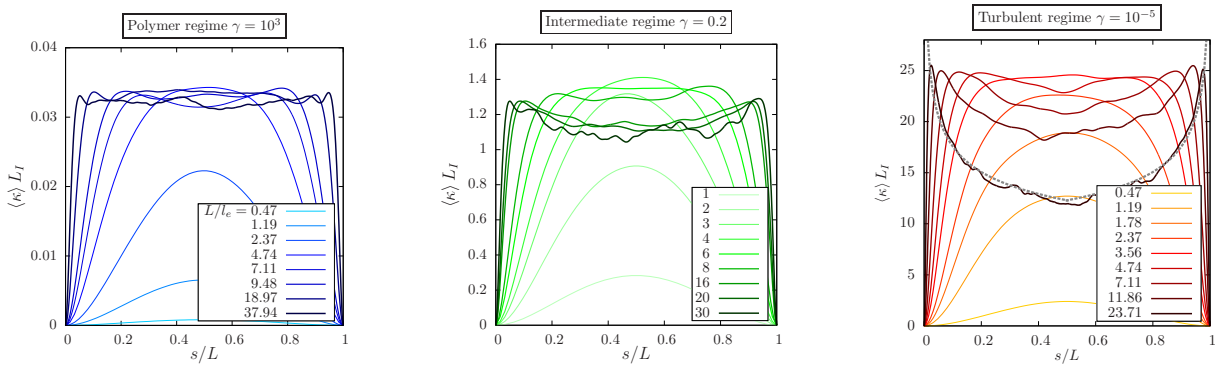

Fig. 4: Evolution of the local mean curvature $\langle\kappa(s)\rangle$ for fibres of increasing length L as a function of the normalised curvilinear coordinate s/L. From left to right, the polymer regime ($\ell_e \approx 4.2L_I$), intermediate regime ($\ell_e \approx 0.5L_I$) and turbulent regime ($\ell_e \approx 0.042L_I$). The fiber lengths L/ℓ_e for each curve are given in the legends. The dashed line in the third graph represents the scaling law (13).

in the experimental data (○) which are in the intermediate regime. This shows that the forcing correlation is at the origin of a surprising result: long fibres are statistically less curved than shorter ones. As will be demonstrated below, this unexpected straightening of flexible fibres as their length increases is due to two physical ingredients: inextensibility and cumulative viscous effects.

In the following, we derive a scaling to describe more quantitatively this decrease thanks to a power budget similar to the one used to determine the elastic length ℓ_e [19]. For the derivation of the elastic length, an eddy with a size comparable to the fibre length is considered. Here, the deformation is local meaning that $\kappa L \gg 1$ and, hence, the only characteristic length remaining is the characteristic size of the deformation κ^{-1}. Therefore in the power budget the turbulent power available scales as $P_{\text{turb}} \sim \rho_f \kappa^{-3}\epsilon$. As the fibre is inextensible, the local deformation at the curvilinear coordinate s is accompanied by a global rearrangement of the fibre conformation. This rearrangement is at the origin of an additional viscous dissipation. For an infinite fibre, two scenarios are possible. For the first one, the creation of the deformation of size κ^{-1} is fast, meaning that it evolves on a timescale smaller than the bending relaxation time of a fibre of length s. In that case, the global conformation can be considered as frozen and the fibre displacement induced by the local deformation is everywhere parallel to the tangent vector. In the second case, the creation of the deformation of size κ^{-1} is slow, then the global conformation can change and a sweeping phenomenon may occur. The characteristic timescale of the formation of the deformation κ is given by $\tau_v(\kappa^{-1}) \sim \eta\kappa^{-4}/B$ and the one of the global rearrangement is given by $\tau_v(s) \sim \eta s^4/B$ [10]. Then, for curvature high enough (such that $\tau_v(\kappa^{-1}) \ll \tau_v(s)$), the conformation can indeed be considered as frozen. For fibre with finite length the reconfiguration should occur on the smallest part of the fibre to minimise the dissipation ($[0:s]$ if $s < L/2$ or $[s:L]$ if $s > L/2$). For a deformation occurring at a curvilinear coordinate s ($s < L/2$), the average viscous dissipation P_v due to the global rearrangement can be written as

$$P_v(s) = \left\langle \int_0^s \eta \boldsymbol{u}_{\text{slip}} \cdot \partial_t \boldsymbol{r}(s',t))_{\parallel} \, \mathrm{d}s' \right\rangle , \qquad (11)$$

where $\partial_t \boldsymbol{r}(s',t))_{\parallel} = (\partial_t \boldsymbol{r}(s',t) \cdot \boldsymbol{t})\, \boldsymbol{t}$ is the tangent velocity of the center line. Given that the fibre is inextensible, the norm of the tangent velocity $|\partial_t \boldsymbol{r}(s',t))_{||}|$ is constant along the fibre and scales with $1/(\kappa\tau_v(\kappa^{-1}))$. Thus, the average dissipated power can be rewritten as

$$P_v(s) \simeq \frac{\eta}{\kappa\tau_v} \int_0^s u_{\parallel}(s')\mathrm{d}s' , \qquad (12)$$

where $u_{\parallel} = \boldsymbol{u}_{\text{slip}} \cdot \boldsymbol{t}$. In a turbulent flow, it was shown for a sphere of diameter d in the inertial range that the slipping velocity scales as $(\epsilon d)^{1/3}$ [33]. By analogy, the integral (12) can be approximated by $u_s s$ where $u_s \sim (\epsilon s)^{1/3}$ is the typical velocity of an eddy of size s. The contribution of the smallest eddies cancels out as they are not correlated over the distance s. Hence, the dissipative power at scale s scales as $P_v \sim \eta/(\kappa\tau_v) s u_s$. So for long fibres and $s \gtrsim \ell_e$, the turbulent power $P_{\text{turb}} = \rho_f \kappa^{-3}\epsilon$, is balanced by the cumulative viscous power P_v, the bending power being negligible. Thus, the curvature $\kappa(s)$ should scale as

$$\langle\kappa(s)\rangle \propto s^{-2/9} . \qquad (13)$$

Note that even though equation (1) is local, the cumulative effect of the viscous drag along the fibre is present through the tension term $\partial_s (T\partial_s \boldsymbol{r})$ which ensures the fibre inextensibility.

For the polymer regime where the elastic length is larger than the integral scale, this additional term also exists. However, the slipping velocity is here a random delta correlated variable. So, the integral (12) vanishes and only the bending term in the power balance remains.

The influence of this additional friction term is highlighted in fig. 4 which represents, for the three regimes,

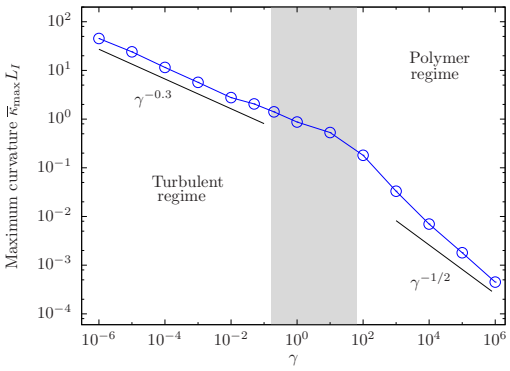

Fig. 5: Evolution of the maximum of the mean curvature $\bar{\kappa}_{\max}$ as a function of the fibre stiffness γ. The grey area corresponds roughly to the intermediate regime ($\ell_e/L_I \in [10^{-1}, 10]$). The power law in the turbulent regime corresponds to equation (16). The power law in the polymer regime corresponds to a balance between thermal and bending energies.

the evolution of the local mean curvature $\langle \kappa(s) \rangle$ as a function of the curvilinear coordinate s from the numerical model only. While the experimental data also shows a global straightening of the fibres as their lengths increases, equation (13) is only valid when there is clear scale separation between the fibre length and the integral scale which is not the case experimentally. The boundary conditions (no torque and no force at the extremities) impose that the curvature is zero at the extremities. For all the regimes, the curvature increases with the curvilinear coordinate from the extremities until it reaches a maximum for $s \sim \ell_e$. In the turbulent case (fig. 4 on the right), for fibres long enough, the mean curvature decreases for $\ell_e \lesssim s \lesssim L/2$ due to the additional dissipation term that dominates the bending term in the power budget. The scaling proposed in equation (13) is in good agreement for the longest fibre $L = 23.71\, L_I$. For the polymer regime, the delta correlation of the forcing leads to no additional dissipation and the mean local curvature is constant along the profile as shown in fig. 4 on the left. This behaviour is similar to the one observed for worm-like chain polymers in ideal solvent [34]. For the intermediate case (fig. 4 in the middle), the evolution of the local curvature is a mix of these two regimes. For long fibres, the mean local curvature decreases for $\ell_e \lesssim s \lesssim L_I$ and then saturates as the forcing is no more correlated at larger scales.

We finally focus on the maximal amplitude of the mean local curvature $\bar{\kappa}_{\max}$ that can be reached for fibres with a length L greater than ℓ_e. We notice in fig. 3 that the elastic length ℓ_e properly estimates the typical length at which the maximum of the curvature is reached. However, the amplitude of this maximum does not scale with the elastic length. In fig. 5, we report the evolution of the maximum of the dimensionless mean curvature $\bar{\kappa}_{\max} L_I$ as a function of the dimensionless rigidity γ. We varied numerically γ from 10^{-6} to 10^6, leading to $\ell_e/L_I \in [0.02, 23.7]$ in order to continuously transit from the turbulent regime to the polymer regime. As expected, two different power laws are observed, one for each asymptotic regime. We first analyse the turbulent regime. We have seen that the fibre inextensibility, and so the lineic tension along the fiber, plays a key role to understand the decrease of the curvature profile for long fibres. We now show that the fibre inextensibility also determines the maximum of the amplitude of the curvature. The tension term ensuring the fibre inextensibility in equation (1) is actually composed of two terms [13]:

$$\partial_s(T\partial_s \boldsymbol{r}) = \partial_s \left[(T_t - B\kappa^2)\partial_s \boldsymbol{r} \right] , \tag{14}$$

where T_t is the classical tangential force whereas $B\kappa^2$ is necessary to satisfy the inextensibility constraint when the fibre is curved. The term $\partial_s \left(B\kappa^2 \partial_s \boldsymbol{r} \right)$ has one component parallel to the tangent vector, $B\partial_s(\kappa^2)\partial_s \boldsymbol{r}$, and one parallel to the curvature vector, $B\kappa^3 \boldsymbol{e}_\kappa$, where $\boldsymbol{e}_\kappa = \partial_s^2 \boldsymbol{r}/|\partial_s^2 \boldsymbol{r}|$. This last term is parallel to the classical bending term $B\partial_s^4 \boldsymbol{r}$ and may be larger than the linear term for large amplitudes, typically $\kappa > 1/\ell_e$. In that case, the saturation occurs when the nonlinear term $B\kappa^3$ is of the order of the forcing term $\eta u_\ell \sim \eta(\epsilon \ell)^{1/3}$. The length scale ℓ to consider corresponds to the size of the eddy that is responsible for the deformation at $s = \ell_e$, *i.e.* ℓ_e. Thus the following equilibrium can be written

$$B\bar{\kappa}_{\max}^3 \sim \eta(\epsilon \ell_e)^{1/3} \tag{15}$$

Using equation (7), the maximum of curvature should scale as:

$$\bar{\kappa}_{\max} \sim \gamma^{-11/36} St^{-23/72} \sim \gamma^{-0.3} St^{-0.3} . \tag{16}$$

This power law is in good agreement with our observation as shown in fig. 5. For the polymer regime, the forcing is not correlated at the scale of the deformation. Hence, the amplitude of the curvature is expected to be weak, as observed in fig. 3. The saturation is then expected to be related to the balance between the "thermal energy" $\rho_f (L/L_I) L_I^3 U^2$ with the bending energy $BL\bar{\kappa}^2$ leading to $\bar{\kappa}_{\max} \sim \gamma^{-1/2}$. The "thermal energy" $\rho_f (L/L_I) L_I^3 U^2$ is the sum of the energy brought by each eddy of size L_I along the fibre. This scaling seems compatible for the largest values of γ we have tested ($\gamma > 10^4$). Note that the case presented in fig. 5 is not in this asymptotic regime yet. This is due to the scale separation between the elastic length and the integral scale which is not large enough, as mentioned previously. Note also that in polymer science the elastic energy stored in the fibre is generally related to the persistence length: $\mathcal{E}_{el} = \int B\kappa^2 \mathrm{d}s \sim B/\ell_p$ and the persistence length to the fibre curvature $\ell_p \sim \bar{\kappa}^{-1}$ [35], should lead to $\bar{\kappa} \sim \gamma^{-1}$. Understanding the discrepancy between this simple argument and our measurement is beyond the scope of this paper and will be investigated later.

Conclusion. We performed a detailed study focusing on the mean curvature of deformable fibres in turbulent

flows. Three different regimes were identified: the polymer regime ($L_I \ll \ell_e < L$), the intermediate regime ($\ell_e \lesssim L_I < L$) and the turbulent regime ($\ell_e < L < L_I$). We showed that the differences between these regimes are related to the temporal and spatial correlations of the turbulence. In a first regime, a fibre in a turbulent flow can be analogous to a polymer in a thermal bath, leading to a maximum curvature independent of the fibre length. In the turbulent regime however, which is the main focus of this paper, we observe a straightening of the fibre as the mean curvature decreases when the fibre length increases, an effect ultimately due to a combination of the fiber inextensibility and the spatial correlation of the forcing through the cumulative viscous forces along the fibre. Finally, the intermediate regime is a combination of these two previous cases in which the flow is correlated at small scales and uncorrelated for the largest deformations.

In the future, the importance of the fibre inertia, measured by the Stokes number St here, needs to be addressed. Due to the many simplifying assumptions used to derive the numerical model used here, further comparative studies using DNS of the Navier–Stokes equations, fully coupled with the elastic dynamics of the fibre, are a natural next step. Improving the experimental apparatus in order to reach the turbulent regime, by using a more flexible material for the fibres and a larger tank, would also be valuable. Finally, the statistics of the deformation should be investigated further to see how the different quantities discussed in this letter fluctuate around their mean values. These fluctuations can have a major impact on the transport of particles, especially for brittle objects for which large curvatures may be responsible for their fragmentation. Once the deformations are fully characterised in each regime, studying the fibre dynamics is the next step to model the transport of flexible objects in turbulence.

This work was carried out in the framework of FlexFiT Project (ANR-17-CE30-0005-01) funded by the French National Research Agency (ANR), the Labex MEC Project (No. ANR-10-LABX-0092) and of the A*MIDEX Project (No. ANR-11-IDEX-0001-02), funded by the *Investissements d'Avenir* French Government program managed by the French National Research Agency (ANR).

REFERENCES

[1] Lundell F., Soderberg L. and Alfredsson P., *Annu. Rev. Fluid Mech.*, **43** (2011) 195.
[2] Nguyen H. and Fauci L., *J. R. Soc. Interface*, **11** (2014) 20140314.
[3] Sabban L. and van Hout R., *J. Aerosol Sci.*, **42** (2011) 867.
[4] Toschi F. and Bodenschatz E., *Annu. Rev. Fluid Mech.*, **41** (2009) 375.
[5] Voth G. and Soldati A., *Annu. Rev. Fluid Mech.*, **49** (2017) 249.
[6] Parsa S., Calzavarini E., Toschi F. and Voth G., *Phys. Rev. Lett.*, **109** (2012) 134501.
[7] Byron M., Einarsson J., Gustavsson K., Voth G., Mehlig B. and Variano E., *Phys. Fluids*, **27** (2015) 035101.
[8] Lindström S. B. and Uesaka T., *Phys. Fluids*, **19** (2007) 113307.
[9] Delmotte B., Climent E. and Plouraboué F., *J. Comput. Phys.*, **286** (2015) 14 .
[10] Powers T., *Rev. Mod. Phys.*, **82** (2010) 1607.
[11] Antman S. S., *Nonlinear Problems of Elasticity* (Springer-Verlag New York) 1995.
[12] Lindner A. and Shelley M., *Elastic fibers in flows* in *Fluid-Structure Interactions in Low-Reynolds-Number Flows* (Royal Society of Chemistry) 2015 pp. 168–192.
[13] Marheineke N. and Wegener R., *SIAM J. Appl. Math.*, **66** (2006) 1703.
[14] Liverpool T. B., *Phys. Rev. E*, **72** (2005) 021805.
[15] Marhieneke N. and Wegener R., *Int. J. Multiphas. Flow*, **37** (2011) 136.
[16] Guazzelli E. and Morris J. F., *A physical introduction to suspension dynamics* Vol. 45 (Cambridge University Press) 2011.
[17] Frisch U., *Turbulence* (Cambridge University Press) 1995.
[18] Yamakawa H., *Modern Theory of Polymer Solutions* (Harper & Row, Publishers) 1971.
[19] Brouzet C., Verhille G. and Le Gal P., *Phys. Rev. Lett.*, **112** (2014) 074501.
[20] Verhille G. and Bartoli A., *Exp. Fluids*, **57** (2016) 117.
[21] Qureshi N., Bourgoin M., Baudet C., Cartellier A. and Gagne Y., *Phys. Rev. Lett.*, **99** (2007) 184502.
[22] Tornberg A.-K. and Shelley M. J., *J. Comput. Phys.*, **196** (2004) 8 .
[23] Huang X.-X., Shin S. J. and Sung H. J., *J. Comput. Phys.*, **226** (2007) 2206 .
[24] Li L., Manikantan H., Saintillan D. and Spagnolie S. E., *J. Fluid Mech.*, **735** (2013) 705–736.
[25] Ascher U. M., Ruuth S. J. and Wetton B. T. R., *SIAM J. Numer. Anal.*, **32** (1995) 797.
[26] Favier J., Revell A. and Pinelli A., *J. Comput. Phys.*, **261** (2014) 145 .
[27] Fung J., Hunt J., Malik N. and Perkins R., *J. Fluid Mech.*, **236** (1992) 281–318.
[28] Kraichnan R. H., *Phys. Fluids*, **13** (1970) 22.
[29] Fung J. and Vassilicos J., *Phys. Rev. E*, **57** (1998) 1677.
[30] Malik N. A. and Vassilicos J. C., *Phys. Fluids*, **11** (1999) 1572.
[31] Favier B., Godeferd F. S. and Cambon C., *Phys. Fluids*, **22** (2010) 015101.
[32] Keller J. and Rubinow S., *J. Fluid Mech.*, **75** (1976) 705–714.
[33] Cisse M., Homann H. and Bec J., *J. Fluid Mech.*, **735** (2013) R1.
[34] Hsu H.-P., Paul W. and Binder K., *Europhys. Lett.*, **92** (2010) .
[35] Hallatschek O., Frey E. and Kroy K., *Phys. Rev. E*, **75** (2007) 031905.